Valley current splitter in minimally twisted bilayer graphene

Tao Hou,[1,2] Yafei Ren,[1,2] Yujie Quan,[1,2] Jeil Jung,[3] Wei Ren,[4] and Zhenhua Qiao[1,2,*]
[1]*ICQD, Hefei National Laboratory for Physical Sciences at Microscale, University of Science and Technology of China, Hefei, Anhui 230026, China*
[2]*CAS Key Laboratory of Strongly-Coupled Quantum Matter Physics, and Department of Physics, University of Science and Technology of China, Hefei, Anhui 230026, China*
[3]*Department of Physics, University of Seoul, Seoul 02504, South Korea*
[4]*International Centre for Quantum and Molecular Structures, Materials Genome Institute, Shanghai Key Laboratory of High Temperature Superconductors, Physics Department, Shanghai University, Shanghai 200444, China*

(Received 30 April 2020; revised 18 July 2020; accepted 11 August 2020; published 27 August 2020)

We study the electronic transport properties at the intersection of three topological zero lines as the elementary current partition node that arises in minimally twisted bilayer graphene. Unlike the partition laws of two intersecting zero lines, we find that (i) the incoming current can be partitioned into both left-right adjacent topological channels and (ii) the forward-propagating current is nonzero. By tuning the Fermi energy from the charge-neutrality point to a band edge, the currents partitioned into the three outgoing channels become nearly equal. Moreover, we find that the current partition node can be designed as a perfect valley filter and energy splitter controlled by electric gating. By changing the relative electric-field magnitude, the intersection of three topological zero lines can transform smoothly into a single zero line, and the current partition can be controlled precisely. We explore the available methods for modulating this device systematically by changing the Fermi energy, the energy gap size, and the size of the central gapless region. The current partition is also influenced by magnetic fields and the system size. Our results provide a microscopic depiction of the electronic transport properties around a unit cell of minimally twisted bilayer graphene and have far-reaching implications in the design of electron-beam splitters and interferometer devices.

DOI: 10.1103/PhysRevB.102.085433

I. INTRODUCTION

Twisted van der Waals layers provide intriguing platforms to investigate novel physics. On one hand, twisted bilayer graphene (t-BG) systems provide ideal platforms to explore the electronic correlation effect on the flat bands at magic angles [1–6]. On the other hand, when the twist angle decreases from the magic angles, the reconstruction of atomic lattices in t-BG becomes more and more important [7]. As a result, the incommensurate moiré structure at the magic angles will gradually become an array of commensurate domains with soliton boundaries. The presence of a minimal twist changes the local stacking order, arranging the AB/BA stacking regions periodically in space. The perpendicular electric field in t-BG or the sublattice potential difference in a graphene/h-BN bilayer leads to an energy gap that results in opposite valley Chern numbers at the AB/BA stacking regions. At the interfaces between different topological regions, topologically confined states (i.e., zero-line modes; ZLMs) appear and form networks [24–35]. Recently, a network of topologically protected helical states was discovered in minimally twisted bilayer graphene [7–21] and graphene/hexagonal boron nitride (h-BN) superlattices [22,23]. Because of the threefold rotational symmetry of the lattices, the elementary component of this network is the intersection of three ZLMs. In contrast to pristine atomic crystals where the electrons can be regarded as a particle hopping from one site to another, the electrons in a topological network are more like a wave propagating along the domain wall without distribution inside the domains. Thus, novel transport properties are expected. However, the microscopic electronic transport properties of this intersecting point remains poorly understood.

In this paper, we study the transport properties of three intersecting ZLMs connected to six terminals. When current is injected from one terminal, we find notable partitioning towards the forward channel; this situation is qualitatively different from the intersection of two ZLMs, where no forward propagation of current is observed. In the case of three intersecting ZLMs, the incoming current is partitioned towards the forward and the two adjacent zero lines. This current partitioning depends strongly on the size of the central region when the region is small but saturates when it is large. By tuning the Fermi level, we find that the current partition can be controlled over a wide range. A perpendicular magnetic field can tune the currents propagating to the adjacent lines, whereas the forward-propagating current remains quite robust. By changing the size of the AA stacking zone, we also study the effect of a twist angle on the transport properties. We find that (i) our device can support stable current partitioning even without a perpendicular electric field and (ii) the electric field allows us to tune the partition properties and turn the device into a valley current splitter.

*qiao@ustc.edu.cn

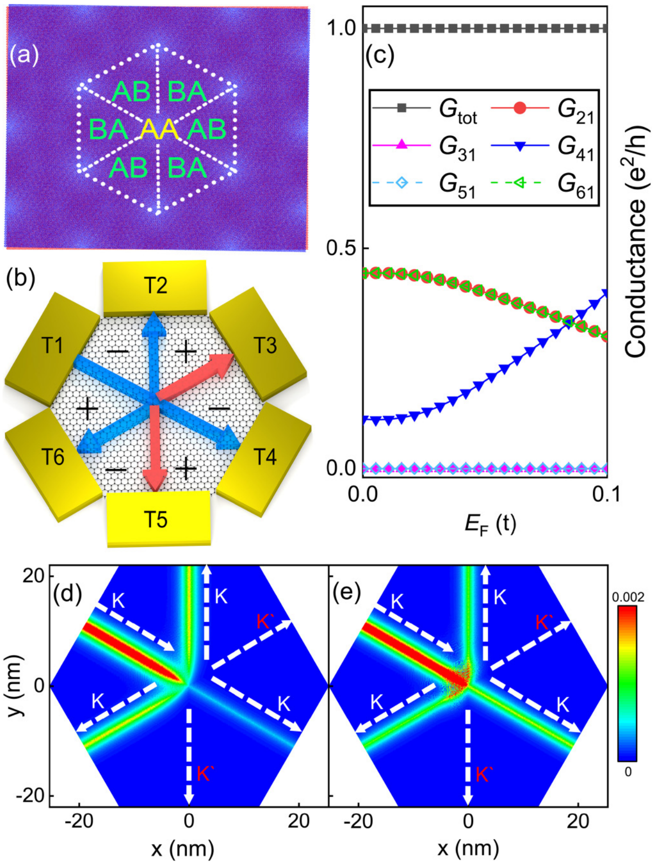

FIG. 1. (a) Moiré pattern of twisted bilayer graphene and identification of regions with AB, BA, and AA stacking. (b) Schematic of six-terminal device with three intersecting zero lines. The plus and minus signs indicate the alternating sublattice potentials. Throughout this paper and unless specified otherwise, we use a side length of 25 nm for our regular hexagonal device. Blue and red arrows correspond to modes that carry valley indices K and K', respectively. Transmission is forbidden along the zero lines with reversed chirality indicated by the red arrows. (c) Dependence of current partitioning as a function of the Fermi level to the different output terminals. G_{j1} is the conductance between T_1 and T_j, while G_{tot} is the total conductance between T_1 and all the other terminals, which remains quantized when the Fermi level shifts from the charge-neutrality point and gradually approaches the bulk gap edge. (d, e) Local density of states of incoming current at Fermi level energies $10^{-3}t$ and $0.1t$, respectively. Green arrows show the forward propagation directions of valley K currents, while white arrows represent the zero lines with valley index K' where the currents do not propagate. The color bar shows the linear gradient of values.

II. MODEL HAMILTONIAN

The general stacking order of the moiré pattern is shown in Fig. 1(a), where the bright zone in the center corresponds to AA stacking. The size of the AA stacking region decreases with a decrease in the twist angle. Around this central zone, alternating periodic chiral AB or BA stacking regions are formed. At the interfaces between the AB and the BA stacking regions, domain walls appear, indicated by the dashed white lines. By applying a perpendicular electric field, the centers of the chiral stacking regions become gapped, while gapless ZLMs form at the domain walls [8,15,16]. The AA stacking zone is located at the intersection of three concurrent ZLMs, which are successively rotated by 60°. Without loss of generality, in our calculations we consider a monolayer graphene flake with position-dependent staggered sublattice potentials to form six adjacent regions with different valley Hall topologies labeled by plus/minus signs in Fig. 1(b), which correspond to AB/BA stacking regions under an electric field in a twisted bilayer graphene. The valley Hall domain walls form three intersecting zero lines, while the intersection region corresponding to the AA stacking zone in the moiré pattern of a twisted bilayer is not gapped locally. The monolayer graphene flake with staggered site potentials can be described by the π-orbital tight-binding Hamiltonian

$$H = -t\sum_{\langle ij\rangle} c_i^\dagger c_j + \sum_{i\in A} U_{Ai} c_i^\dagger c_j + \sum_{i\in B} U_{Bi} c_i^\dagger c_j,$$

where $c_i^\dagger$ (c_i) is a creation (annihilation) operator for an electron at site i, and $t = 2.6\,\mathrm{eV}$ is the nearest-neighbor hopping amplitude. The sublattice potentials are spatially varying, with $U_{Ai} = -U_{Bi} = \lambda\Delta$ in regions labeled by $\lambda = \pm$ as shown in Fig. 1(b), where 2Δ measures the magnitude of the staggered sublattice potential difference.

The zero lines are connected to six reservoirs labeled T_i (i = 1-6) as shown in Fig. 1(b). Herein, we take T_1 to be the injection terminal. The electronic transport calculations are based on the Landauer-Büttiker formula [36] and recursively constructed Green's functions [37]. The conductance from the q terminal to the p terminal is evaluated from

$$G_{pq} = \frac{2e^2}{h}\mathrm{Tr}[\Gamma_p G^r \Gamma_q G^a],$$

where $G^{r,a}$ is the retarded/advanced Green's function of the central scattering region, and Γ_p is the line-width function describing the coupling between the p terminal and the central scattering region. The propagation of a ZLM coming in from the p terminal is illustrated by the local density of states at energy ϵ, which can be calculated by

$$\rho_p(r,\epsilon) = 1/2\pi[G^r\Gamma_p G^a]_{rr},$$

where r is the actual spatial coordinate.

III. RESULTS AND DISCUSSION

A. Current partition laws

In our calculations, the central region is a hexagon with circumcircle diameter $D = 50$ nm, and the diameter of the AA stacking zone is 0.28 nm unless stated otherwise. With $\Delta = 0.1t$, we calculate how the current partition depends on the Fermi energy E_F as shown in Fig. 1(c). The current partition laws can be summarized as

$$G_{31} = G_{51} = 0, \tag{1}$$

$$G_{21} = G_{61}, \tag{2}$$

$$G_{tot} = G_{21} + G_{41} + G_{61} = e^2/h. \tag{3}$$

Here, Eq. (1) restricts current partitioning into zero lines of opposite chirality, while the condition in Eq. (2) requires the mirror reflection symmetry of the partition, which is broken in the presence of a magnetic field as we show later. Equation (3) implies that there is no backscattering due to intervalley scattering, and indeed any reflected current remains very weak even in the presence of disorders [26].

Note that the forward-propagating conductance G_{41} is nonzero because the zero line from T_1 to T_4 has the same chirality, in contrast to the case of two intersecting zero lines, where the forward propagation is forbidden by the chirality conservation rule. Moreover, the forward-current transmission strongly depends on E_F as shown in Fig. 1(c). When E_F is close to the charge-neutrality point (CNP), $G_{41} \approx 0.11e^2/h$ is less than the conductance of $G_{21} = G_{61} \approx 0.44e^2/h$ towards the sides. When E_F is shifted away from the CNP and moves toward the bulk band edges, G_{41} increases gradually and exceeds G_{21} when $E_F > 0.08t$. The current partition at different E_F values is shown more clearly in Figs. 1(d) and 1(e), wherein the local density of states for current injected from T_1 is plotted at $E_F = 0.001t$ and $0.100t$, respectively. This Fermi-energy dependent current partition is because the AA stacking region is not gapped locally, which can be seen as a finite potential barrier located at the zero-lines intersection. Hence, with respect to quantum mechanics, when we increase the Fermi energy, the energy of injecting electrons will also increase, which improves the probability of electrons transmitting the finite potential barrier (AA stacking region). In other words, more injecting current will transmit the AA stacking region and propagate to T_4 when we increase the Fermi energy; meanwhile, the current portioned to T_2 and T_6 will decrease, which suggests that longitudinal transport may be greatly modified through a perpendicular electric gate by altering the current percolation properties through multiple partition nodes.

B. Influence of a magnetic field

In addition to control through electrical means, the current partition is also strongly affected by applying a magnetic field. The effect of a magnetic field $\mathbf{B} = \nabla \times \mathbf{A}$ can be included by attaching a Peierls phase factor to the hopping term

$$t_{i,j} \longrightarrow t_{i,j} \exp\left(-i\frac{e}{\hbar}\int \mathbf{A}\cdot \mathrm{d}l\right),$$

where $\int \mathbf{A}\cdot \mathrm{d}l$ is the integral of the vector potential along the path from site i to site j. The presence of a magnetic field changes the current partition as shown in Fig. 2(a) for $\Delta = 0.1t$ and $E_F = 0.001t$. We find that the presence of the magnetic field removes the equality between G_{21} and G_{61} because the magnetic field breaks the mirror reflection symmetry. However, the forward-propagating current remains unaffected.

By changing E_F under a given magnetic field as shown in Fig. 2(b), we find that the current partitions to both the forward and the side directions vary simultaneously. As E_F approaches the bulk band edge, the current partitioned to T_4 increases gradually but does not reach the same magnitude as that for vanishing magnetic flux. Figures 2(c) and 2(d) show more clearly the current partition under a magnetic flux of $\Phi_B = 0.05$ μWb for $E_F = 0.001t$ and $0.1t$, respectively, wherein more current is partitioned into T_2 than into T_6. This difference is more obvious at the higher Fermi energy, in agreement with previous work [18,19].

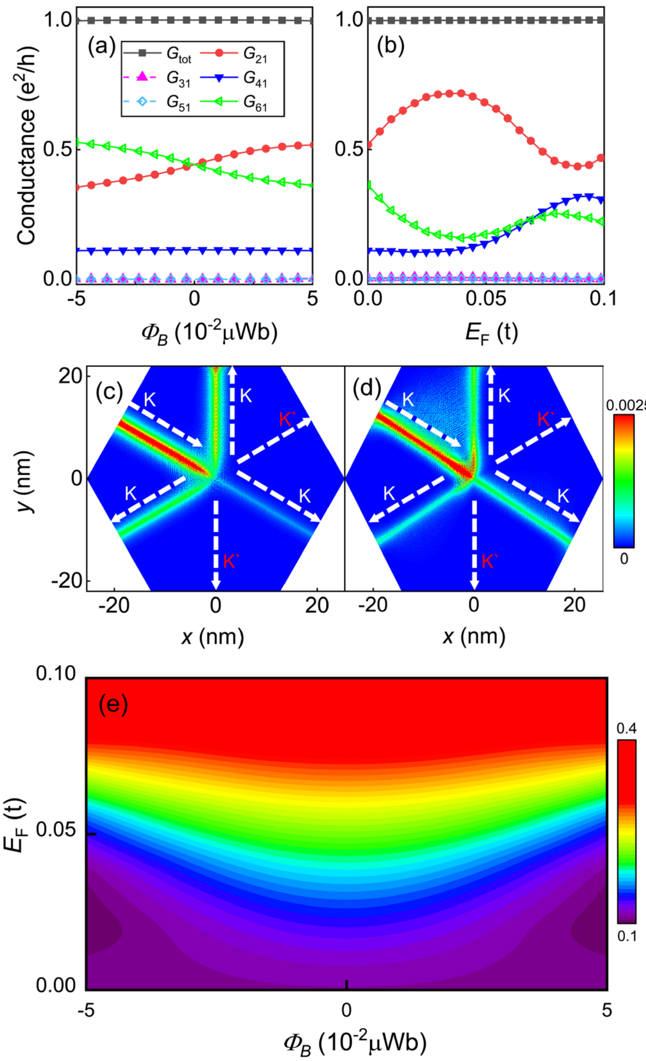

FIG. 2. (a) Conductance near the charge-neutrality point $E_F = 0.001t$ for different values of the magnetic flux Φ_B. (b) Conductance under the same magnetic flux Φ_B for different values of the Fermi energy E_F. (c, d) Local density of states of the injected current for Fermi levels $10^{-3}t$ near the charge-neutrality point and $0.1t$ near the bulk band edge with magnetic flux 0.05 μWb, which illustrates the asymmetric partition of currents towards the side leads. (e) Phase diagram for conductance G_{14} with different values of E_F and Φ_B for $\Delta = 0.1t$. The color bar shows the linear gradient of values in units of e^2/h.

To show the influences of the magnetic field and Fermi energy more systematically, in Fig. 2(e) we show the phase diagram for conductance G_{41} with different values of E_F and Φ_B. G_{41} is only weakly dependent on the magnetic field as E_F approaches the CNP and the bulk band edges but is strongly dependent on the magnetic field in the middle region.

C. Effect of system size

For an electronic nanodevice, its size plays a crucial role. Herein, we investigate the current partition of a device whose

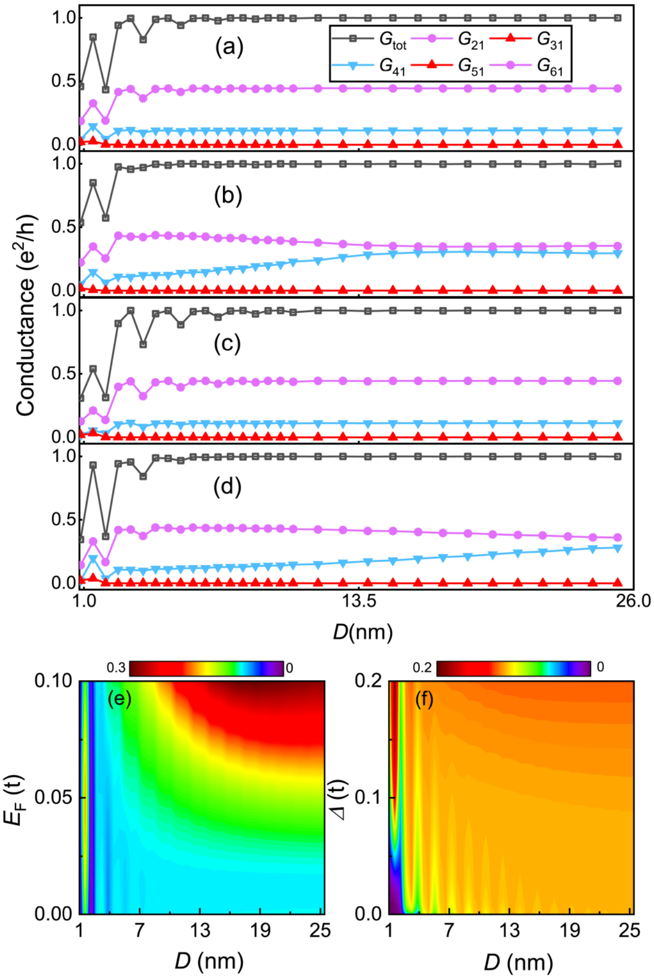

FIG. 3. Dependence of current partitioning on the device circumcircle diameter D for different output leads with (a) potential $\Delta = 0.1t$ and Fermi energy $E_F = 0.001t$, (b) $\Delta = 0.1t$ and $E_F = 0.1t$, (c) $\Delta = 0.05t$ and $E_F = 0.001t$, and (d) $\Delta = 0.05t$ and $E_F = 0.05t$. Phase diagrams for conductance G_{41} with (e) different values of E_F and L but the same potential $\Delta = 0.1t$ and (f) different values of Δ and L but the same Fermi energy $E_F = 0.001t$. The color bar shows the linear gradient of values in units of e^2/h.

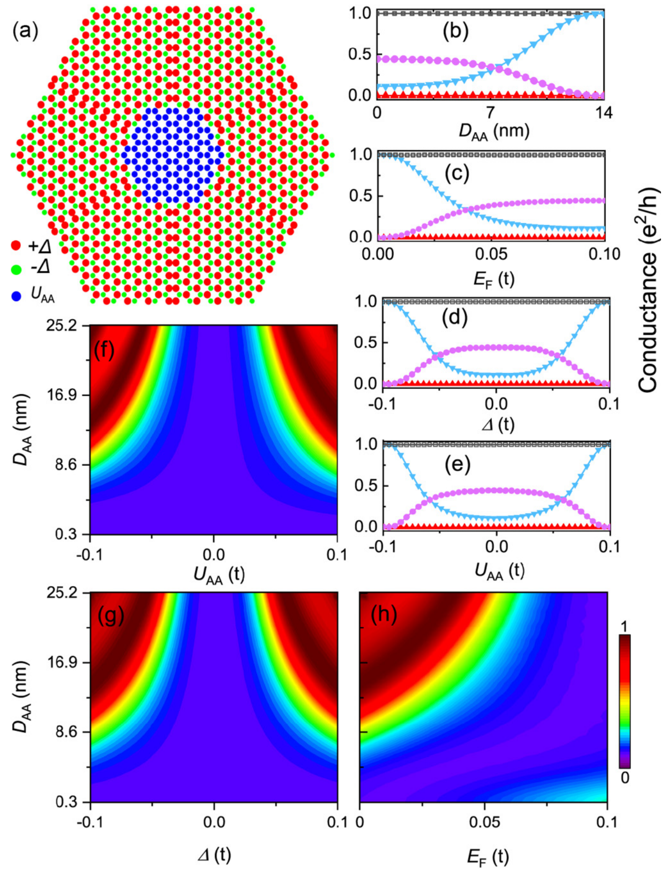

FIG. 4. (a) Schematic of the lattice structure. Red (green) points are lattice points with a positive (negative) potential Δ, and blue points are lattice points with potential U_{AA}. (b–e) Dependence of the current partition into different outgoing leads (describe the curves) for different sampling of system parameters such as the diameter D_{AA} of the AA stacked zone, Fermi energy E_F, and staggering potentials $\Delta = U_{AA}$, represented as a function of (b) D_{AA} for $E_F = 0.001t$ and $\Delta = U_{AA} = 0.1t$, (c) E_F for $D_{AA} = 14$ nm and $\Delta = U_{AA} = 0.1t$, (d) Δ for D_{AA} nm, $E_F = 0.001t$, and $U_{AA} = \Delta$, and (e) U_{AA} for $D_{AA} = 14$ nm, $E_F = 0.001t$, and $\Delta = 0.1t$. (f) Phase diagram for conductance G_{41} with different values of U_{AA} and D_{AA} for $E_F = 0.001t$ and $\Delta = 0.1t$. (g) Phase diagram for conductance G_{41} with different values of Δ and D_{AA} for $E_F = 0.001t$ and $U_{AA} = \Delta$. (h) Phase diagram for conductance G_{41} with different values of E_F and D_{AA} for $\Delta = U_{AA} = 0.1t$. The color bar shows the linear gradient of values in units of e^2/h, and the current-partitioning labels are the same as in Fig. 3.

circumcircle diameter D ranges from 1 to 25 nm. In Figs. 3(a)–3(d), we plot the current partition as a function of D at different Fermi energies E_F and staggered sublattice potential Δ. The current partition fluctuates obviously for $D < 6$ nm, which is mainly due to the backscattering because the total conductance is not quantized. When the system size L increases, the backscattering vanishes. However, increasing the system size has only a weak influence on the current partition when E_F is close to the CNP but has a definite influence of bringing G_{41} and G_{21} closer together when E_F lies at the band edge. This behavior suggests that the equal-current partition approximation is valid at a small twist angle but invalid at a large twist angle when the Fermi energy E_F is far from charge neutrality.

The length dependence of the current partition at different E_F values with $\Delta = 0.1t$ is shown in Fig. 3(e), wherein the fluctuation appears for small sizes and exhibits a weak dependence on E_F. As the system size increases, G_{41} gradually increases and then saturates at a magnitude that increases with E_F. By setting $E_F = 0.001t$, we plot the phase diagram of G_{41} as a function of the energy gap Δ and circumcircle diameter D in Fig. 3(f), wherein similar behaviors are observed. Moreover, we find that the saturated G_{41} at larger sizes also increases with the energy gap.

D. Effect of AA stacking size

We now study how the AA stacking size at the intersection affects the current partition, as shown schematically in Fig. 4(a). This can simulate the effect of the twisting angle θ in t-BG, where the size of the AA stacking zone shrinks at smaller twist angles θ [38]. In particular, we only consider the twist angle range from 0.1° to 0.2°, in which cases the domains are observable and the domain walls are sharp enough to be described by our model Hamiltonian. We vary the circumcircle diameter of the AA stacking region, namely, D_{AA}, from the smallest size to 25.2 nm while fixing the device size at $D = 50$ nm. At $E_F = 0.001t$ and $\Delta = 0.1t$, we find that G_{41} increases with D_{AA} and becomes quantized at $D_{\text{AA}} \approx 14$ nm, where the current partition of $G_{21,61}$ vanishes. This behavior suggests that the central AA stacking region acts as a scattering zone whose scattering weakens as its size increases, thereby increasing the forward-propagation current. As a result, most of the current flows along one zero line, with weak partition to the other allowed zero lines.

For the largest AA stacking region, i.e., when there is no longer an energy gap in the central scattering region, the current is fully partitioned into the forward-propagating zero line. Upon changing E_F from the CNP, we find that the current partition becomes tunable. As we increase E_F, G_{41} first decreases and then increases to the quantized value near $E_F \approx 0.05t$. When we further increase E_F, G_{41} decreases to a small value. For $D_{\text{AA}} = 14$ nm and $\Delta = 0.1t$, the current partitioned into L_4 increases with $|\Delta|$ and those into L_2 and L_6 decrease. Note that all of the above results were calculated under the condition that $U_{\text{AA}} = \Delta$. At $E_F = 0.001t$ and $\Delta = 0.1t$, we find that G_{41} increases with $|U_{\text{AA}}|$ and becomes quantized at $|U_{\text{AA}}| = \Delta$, where the current partitioning of $G_{21,61}$ vanishes.

In Fig. 4(f), we plot the phase diagram of G_{41} with different U_{AA} and D_{AA} at fixed $E_F = 0.001t$ and $\Delta = 0.1t$; for $D_{\text{AA}} <$ 4.3 nm, U_{AA} no longer influences the current partitioning. In Fig. 4(g), we also plot the phase diagram of G_{41} with different Δ and D_{AA} at fixed $E_F = 0.001t$. Now the resonant transmission appears for a different band gap Δ. As we decrease $|\Delta|$ from $0.1t$, the value of D_{AA} for resonant transmission increases until it equals 25.2 nm, and the resonant transmission disappears when $|\Delta| < 0.6t$. Figure 4(h) plots the phase diagram of G_{41} with different E_F values and D_{AA} at fixed $\Delta = 0.1t$. One finds that the resonant transmission appears at $E_F < 0.05t$ and the resonant diameter increases with E_F. Note that at the resonant transmission point of $\Delta = 0.1t$ and $D_{\text{AA}} \approx 14$ nm, increasing E_F drives G_{41} to decrease gradually as in Fig. 4(c), suggesting that the current partition goes from 0 to a finite value. Such tunability by means of electric gating could be used to construct a field-effect transistor based on the dissipationless topological ZLMs for switching on and off the forward propagation.

E. Tunable valley current splitter

In order to control the current partition effectively and quantitatively, we add two sets of electric fields Δ_1 and Δ_2 to the six-terminal device, as shown in the inset in Fig. 5(a). We vary the magnitude of Δ_2/Δ_1 while fixing $E_F = 0.001t$, the device size $D = 50$ nm, and $\Delta_1 = 0.1t$. We find that G_{41} becomes quantized when $\Delta_2/\Delta_1 < 0$, where the current partition of $G_{21,61}$ vanishes, which means that there exists only a single zero line. With $\Delta_2/\Delta_1 > 0$, we find that G_{41} decreases and $G_{21,61}$ increase with Δ_2/Δ_1. When $\Delta_2/\Delta_1 \approx 0.6$, $G_{41,21,61}$ become the same value. When we further increase

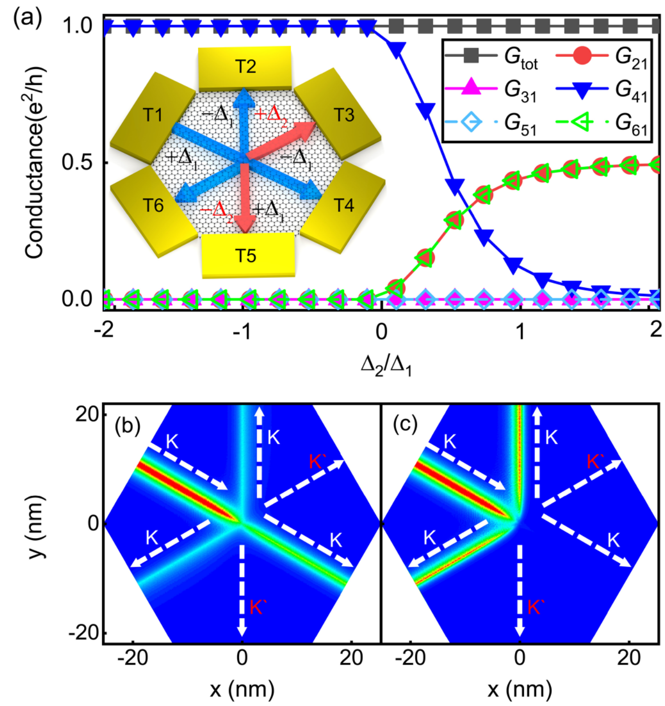

FIG. 5. (a) Dependence of current partitioning as a function of Δ_2/Δ_1 for different output leads with Fermi energy $E_F = 0.001t$. Inset: Schematic of the six-terminal device with two pairs of gates labeled Δ_1 and Δ_2. (b, c) Local density of states of incoming current at $\Delta_2/\Delta_1 = 0.2$ and $\Delta_2/\Delta_1 = 2$, respectively, at the same Fermi level energies, $0.001t$.

Δ_2/Δ_1 to 2, G_{41} decreases to 0 and $G_{21,61}$ become $0.5e^2/h$, as shown in Fig. 5(c), which shows the current partition just like the intersection of two zero lines. By fixing one of the electric fields and varying the other, we can modulate the partition G_{41} from 0 to quantized, precisely, making this device more qualified as a valley current splitter.

IV. SUMMARY

We have presented a systematic study of the electronic transport properties of three intersecting zero lines in a twisted bilayer graphene, which form six topological zones stacked either in AB or in BA patterns and are centered in a gapless region with AA stacking. We have investigated the influence of the system size, AA-region size, E_F, energy gap, and magnetic field on the current partitioning. When current flows through the device, the forward-propagating current partitioning G_{41} is nonzero and can be tuned by mediating E_F. This is in contrast to the topological intersection of two zero lines, where forward propagation is forbidden.

When the central AA region is small, increasing E_F to the band edge enhances G_{41} to partition the current into three nearly equal zero lines, and the potential of the AA region does not affect the current partitioning. By making the central AA region larger, which corresponds to decreasing the twist angle, resonant forward transmission can be realized at a proper E_F, in which case the partitioning to the side zero lines vanishes. Starting from the case of resonant transmission, further increasing E_F (e.g., by means of electric gating) increases the current partitioning to the side zero lines from 0 to a definite level, thereby suggesting that the system could be used as a dissipationless field-effect transistor. Moreover, decreasing the system size gives rise to strong backscattering and conductance fluctuations. In the absence of a magnetic field, the symmetric geometry of our central region leads to $G_{21} = G_{61}$ current partitioning, but the presence of a magnetic field breaks this symmetry.

Our theoretically proposed device can precisely find experimental realization in graphene moiré structures and can also find realizations in phononic crystals. Specifically, our findings are the first prediction of the current partition at the zero-line intersection node of a triangular network of topological channels in small-twist-angle bilayer graphene and pave the way towards the realization of low-power topological quantum devices.

ACKNOWLEDGMENTS

This work was supported financially by the National Key R&D Program (Grant Nos. 2017YFB0405703 and 2016YFA0301700), the NNSFC (Grant Nos. 11474265, and 11674024), the China Government Youth 1000-Plan Talent Program, and the Anhui Initiative in Quantum Information Technologies. We are grateful to the AMHPC and Supercomputing Center of USTC for providing high-performance computing assistance.

[1] Y. Cao, V. Fatemi, S. Fang, K. Watanabe, T. Taniguchi, E. Kaxiras, R. C. Ashoori, and P. Jarillo-Herrero, Nature (London) **556**, 43 (2018).
[2] Y.-Z. Chou, Y.-P. Lin, S. Das Sarma, and R. M. Nandkishore, Phys. Rev. B **100**, 115128 (2019).
[3] J. Liu, Z. Ma, J. Gao, and X. Dai, Phys. Rev. X **9**, 031021 (2019).
[4] M. Koshino, Phys. Rev. B **99**, 235406 (2019).
[5] T. Cea, N. R. Walet, and F. Guinea, Nano Lett. **19**, 8683 (2019).
[6] J. Lee, E. Khalaf, S. Liu, X. Liu, Z. Hao, P. Kim, and A. Vishwanath, Nat. Commun. **10**, 5333 (2019).
[7] H. Yoo, R. Engelke, S. Carr, S. Fang, K. Zhang, P. Cazeaux, S. H. Sung, R. Hovden, A. W. Tsen, T. Taniguchi, K. Watanabe, G. Yi, M. Kim, M. Luskin, E. B. Tadmor, E. Kaxiras, and P. Kim, Nat. Mater. **18**, 448 (2019).
[8] S. Huang, K. Kim, D. K. Efimkin, T. Lovorn, T. Taniguchi, K. Watanabe, A. H. MacDonald, E. Tutuc, and B. J. LeRoy, Phys. Rev. Lett. **121**, 037702 (2018).
[9] P. Rickhaus, J. Wallbank, S. Slizovskiy, R. Pisoni, H. Overweg, Y. Lee, M. Eich, M. Liu, K. Watanabe, T. Taniguchi, V. Fal'ko, T. Ihn, and K. Ensslin, Nano Lett. **18**, 6725 (2018).
[10] S. G. Xu, A. I. Berdyugin, P. Kumaravadivel, F. Guinea, R. Krishna Kumar, D. A. Bandurin, S. V. Morozov, W. Kuang, B. Tsim, S. Liu, J. H. Edgar, I. V. Grigorieva, V. I. Fal'ko, M. Kim, and A. K. Geim, Nat. Commun. **10**, 4008 (2019).
[11] A. Ramires and J. L. Lado, Phys. Rev. Lett. **121**, 146801 (2018).
[12] D. K. Efimkin and A. H. MacDonald, Phys. Rev. B **98**, 035404 (2018).
[13] M. P. Makwana and R. V. Craster, Phys. Rev. B **98**, 235125 (2018).
[14] P. San-Jose and E. Prada, Phys. Rev. B **88**, 121408(R) (2013).
[15] J.-B. Qiao, L.-J. Yin, and L. He, Phys. Rev. B **98**, 235402 (2018).
[16] S. S. Sunku, G. X. Ni, B. Y. Jiang, H. Yoo, A. Sternbach, A. S. McLeod, T. Stauber, L. Xiong, T. Taniguchi, K. Watanabe, P. Kim, M. M. Fogler, and D. N. Basov, Science **362**, 1153 (2018).
[17] T. Hou, Y. F. Ren, Y. J. Quan, J. Jung, W. Ren, and Z. H. Qiao, Phys. Rev. B **101**, 201403(R) (2020).
[18] K. Wang, Y. F. Ren, X. Z. Deng, S. A. Yang, J. Jung, and Z. H. Qiao, Phys. Rev. B **95**, 245420 (2017).
[19] K. Wang, T. Hou, Y. F. Ren, and Z. Qiao, Front. Phys. **14**, 23501 (2019).
[20] J. Li, R. Zhang, Z. Yin, J. Zhang, K. Watanabe, T. Taniguchi, C. Liu, and J. Zhu, Science **362**, 1149 (2018).
[21] J. S. Aldena, A. W. Tsena, P. Y. Huanga, R. Hovdena, L. Brownb, J. Park, D. A. Muller, and P. L. McEuen, Proc. Natl. Acad. Sci. USA **110**, 11256 (2013).
[22] M. Yankowitz, J. Jung, E. Laksono, N. Leconte, B. L. Chittari, K. Watanabe, T. Taniguchi, S. Adam, D. Graf, and C. Dean, Nature **557**, 404 (2018).
[23] H. Kim, N. Leconte, B. L. Chittari, K. Watanabe, T. Taniguchi, A. H. MacDonald, J. Jung, and S. Jung, Nano Lett. **18**, 7732 (2018).
[24] T. Hou, G. Chen, W.-K. Tse, C. Zeng, and Z. Qiao, Phys. Rev. B **98**, 245417 (2018).
[25] I. Martin, Y. M. Blanter, and A. F. Morpurgo, Phys. Rev. Lett. **100**, 036804 (2008).
[26] Z. H. Qiao, J. Jung, Q. Niu, and A. H. MacDonald, Nano Lett. **11**, 3453 (2011).
[27] Z. H. Qiao, J. Jung, C. Lin, Y. F. Ren, A. H. MacDonald, and Q. Niu, Phys. Rev. Lett. **112**, 206601 (2014).
[28] J. Jung, F. Zhang, Z. H. Qiao, and A. H. MacDonald, Phys. Rev. B **84**, 075418 (2011).
[29] Y. T. Zhang, Z. H. Qiao, and Q. F. Sun, Phys. Rev. B **87**, 235405 (2013).
[30] X. T. Bi, J. Jung, and Z. H. Qiao, Phys. Rev. B **92**, 235421 (2015).
[31] C. Lee, G. Kim, J. Jung, and H. Min, Phys. Rev. B **94**, 125438 (2016).
[32] M. Kim, J. H. Choi, S. H. Lee, K. Watanabe, T. Taniguchi, S. H. Jhi, and H. J. Lee, Nat. Phys. **12**, 1022 (2016).
[33] M. Yan, J. Lu, F. Li, W. Deng, X. Huang, J. Ma, and Z. Liu, Nat. Mater. **17**, 993 (2018).
[34] J. Li, K. Wang, Kenton J. McFaul, Z. Zern, Y. F. Ren, K. Watanabe, T. Taniguchi, Z. H. Qiao, and J. Zhu, Nat. Nanotechnol. **11**, 1060 (2016).
[35] L. Ju, Z. Shi, N. Nair, Y. Lv, C. Jin, J. Velasco Jr., H. A. Bechtel, M. C. Martin, A. Zettl, J. Analytis, and F. Wang, Nature **520**, 650 (2015).
[36] S. Datta, *Electronic Transport in Mesoscopic Systems* (Cambridge University Press, Cambridge, UK, 1997).
[37] J. Wang and H. Guo, Phys. Rev. B **79**, 045119 (2009).
[38] L.-J. Yin, J.-B. Qiao, W.-J. Zuo, W.-T. Li, and L. He, Phys. Rev. B **92**, 081406(R) (2015).